

pubs.acs.org/cm Article

Associative Phase Separation of Aqueous π -Conjugated Polyelectrolytes Couples Photophysical and Mechanical Properties

Anna R. Johnston, Sarah L. Perry, and Alexander L. Ayzner*



Cite This: https://dx.doi.org/10.1021/acs.chemmater.0c02424



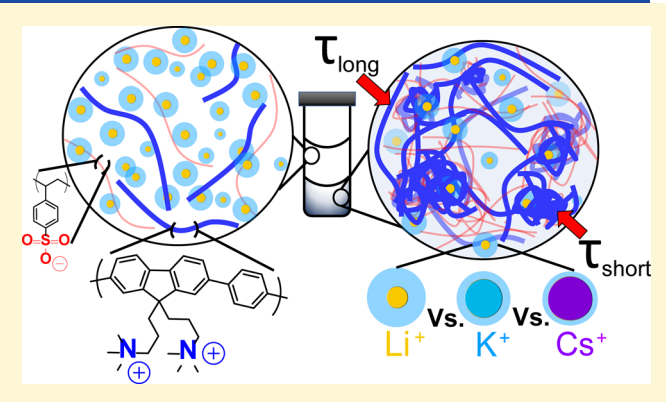
ACCESS

III Metrics & More

Article Recommendations

s Supporting Information

ABSTRACT: The associative phase separation of water-soluble polyelectrolytes is important across many different fields including food science, biomedicine, materials science, and prebiotic organization. Specifically, associative phase separation leading to complex coacervation of oppositely charged polyelectrolytes has been extensively studied to inform research into synthetic cell mimics. However, the phase behavior of conjugated polyelectrolytes (CPEs), macromolecules analogous to chromophores found in light harvesting organelles, has been investigated only minimally. A systematic understanding of the influence of ionic strength on the phase behavior of CPEs could provide insights into the potential for these systems to form complex coacervates and improve control over the photophysical properties of these materials. In this study,



the influence of increasing ionic strength (0–5.0 M) of three simple salts (LiBr, KBr, and CsBr) on the phase behavior of a cationic CPE [poly(fluorene-alt-phenylene)] and an anionic non-conjugated polyelectrolyte [poly(4-styrenesulfonate)] complex is interrogated. Associative phase separation into diluted and concentrated polyelectrolyte phases was found to occur regardless of salt type. We report on the phase composition and influence of the ion type on the photophysical properties of the concentrated phase, where the nature of the counter cation was found to manipulate the radiative decay rate and the exciton diffusion dynamics. Additionally, we demonstrate the ability of the polymer-rich phase to recruit a nonpolar, fullerene-based electron acceptor PC[70]BM, resulting in photoluminescence quenching likely due to photoinduced electron transfer. Our findings show promise for the formation of CPE-based coacervate-like phases and highlight the importance of the interactions of the complex with ions differing in polarizability and size. Additionally, the potential for these systems to form liquid electron donor/acceptor bulk heterojunctions has great implications for their use in optoelectronics.

1. INTRODUCTION

Due to their aqueous solubility and sensitivity to ionic strength, polyelectrolytes have found use in a number of materials and biomedical applications. A remarkable and highly useful property of this class of polymeric materials is their rich phase behavior, which usually depends strongly on the salt concentration. When oppositely charged polyelectrolytes are combined in aqueous solution, they can readily ion-pair to form complexes. This can lead to associative phase separation, thereby forming a dilute solution with a low total polyelectrolyte concentration coexisting with a concentrated phase that is highly enriched in polyelectrolyte complexes. When the concentrated phase is liquid, it is referred to as a polyelectrolyte complex coacervate.

Complex coacervates have been utilized heavily in food science and the personal care industry; more recently, they have been investigated for drug delivery applications, underwater adhesives, and printable electronics. Notably, this phenomenon has also gained interest due to the hypothesis that coacervation may have contributed to early cell development. 8,10,16,17 This hypothesis suggests that phase separation of

charged biological macromolecules led to the formation of membraneless organelles that later became encapsulated by lipid membranes and thus effectively compartmentalized. Coacervation in synthetic systems is currently being studied to better understand early cell development and to inform efforts into the design of synthetic cell mimics.

Unlike most polyelectrolytes under investigation, conjugated polyelectrolytes (CPEs) stand apart due to the presence of polarizable π -electrons, which lead to electronic states that are delocalized along the polymer backbone. This results in a strong dependence of optoelectronic properties such as light absorption, light emission, and excited-state energy migration on the conformation of the CPE chain. We have previously

Received: June 10, 2020 Revised: January 21, 2021



shown that oppositely charged CPEs can be assembled into aqueous complexes in dilute solution, leading to the emergence of new electronic states. The CPEs within the complex were chosen to act as an electronic energy donor/acceptor pair and were shown to support extremely rapid electronic energy transfer on a timescale commensurate with natural chromophore-based antennae found in light-harvesting organelles. ¹⁸

It is intriguing to wonder whether the associative phase separation of CPEs can be used to form concentrated phases that are analogous to non-conjugated polyelectrolyte systems. Doing so would result in a strongly coupled many-body system, where polymer-excited states (excitons) would be able to migrate rapidly between CPE chains within the dense phase. The ionic atmosphere could then be used to judiciously manipulate exciton dynamics, in principle leading to tunable optoelectronic properties in a fluid aqueous system. Realization of such a system is of interest as a membraneless, photophysically active component of an overarching artificial light-harvesting system that mimics a set of core functions of a light-harvesting organelle.

Though complex coacervation using non-conjugated polyelectrolytes continues to be an active area of research, phase behavior in conjugated systems has been studied to a much lesser degree. Danielsen *et al.* studied the associative phase separation of polythiophene-based CPE with a non-conjugated oppositely charged polyelectrolyte in water/tetrahydrofuran (THF) mixtures. Depending on the mixture composition, they reported formation of both coacervate phases and what they referred to as coacervate-precipitates, that is, phases with properties that appear to be intermediate between liquids and solids. However, to the best of our knowledge, aqueous associative phase separation of CPEs in the presence of substantial amounts of excess salt has not been studied to date.

In this report, we interrogate associative phase separation between a model cationic CPE based on a poly(fluorene-alt-phenylene) (PFPI) backbone and a model oppositely charged non-conjugated polyelectrolyte (Figure 1). With increasing

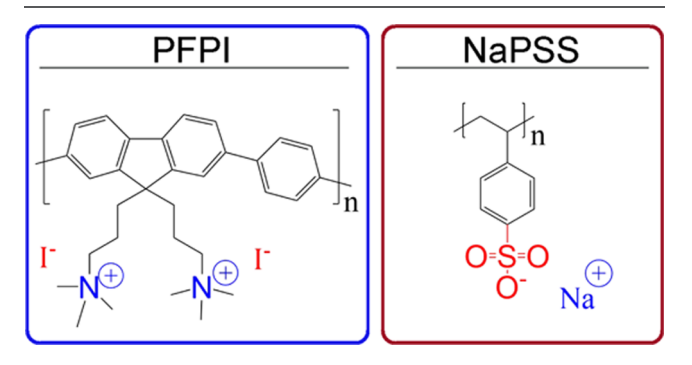


Figure 1. Chemical structures of the conjugated cationic polyelectrolyte, PFPI, and the nonconjugated anionic polyelectrolyte, NaPSS.

ionic strength, we find evidence for the formation of a coacervate-like phase with a microstructure that resembles a colloidal gel. To keep the investigation tractable, we focus on the influence of simple cations (Li⁺, K⁺, and Cs⁺) with a fixed bromide counterion. We then interrogate the phase composition and photophysical properties of the CPE within both the diluted and concentrated phases. Using time-resolved photoluminescence (TRPL) and TRPL anisotropy measurements, we show that the small ion nature and concentration exert a strong influence on the photophysical properties of the

concentrated phase. PL anisotropy dynamics of the dense phase show nonclassical, heterogeneous decay behavior indicative of distinct sub-ensembles of fluorophore environments with differing characteristic PL depolarization times. We find evidence that the desolvation free energy and the polarizability of the cation influence phase behavior of the complex via the cation interaction with the polarizable π electrons of the CPE backbone. Furthermore, we show that the conjugated backbone of the CPE can help recruit nonpolar organic electron acceptors with vanishing aqueous solubilities into the dense phase, leading to PL quenching likely due to photoinduced electron transfer. Our results imply that saltmediated phase separation in CPE-based systems holds substantial promise for the construction of tunable optically active systems in aqueous environments. This system also serve as a testbed to interrogate fundamental many-body interactions between ions and highly delocalized π -electrons.

2. EXPERIMENTAL METHODS

2.1. Sample Preparation. The cationic CPE, PFPI derivative $(M_{\rm W}=21,000~{\rm Da},~{\rm PDI}=1.2)$, was obtained from Solaris Chem Incorporated. The anionic non-conjugated polyelectrolyte, poly(4-styrenesulfonate) (NaPSS) $(M_{\rm W}=\sim 1,000,000~{\rm Da})$, was obtained from Sigma-Aldrich. Phenyl-C71-butyric acid methyl ester (PC[70]BM) was obtained from Ossila. Lithium bromide (LiBr, > 99.0% purity) was obtained from Tokyo Chemical Industries, potassium bromide (KBr, 99.99% purity) was obtained from Sigma-Aldrich, and cesium bromide (CsBr, 99.9% purity) was obtained from Alfa Aesar. Chlorobenzene (spectrometric grade, 99.9% purity) was obtained from Alfa Aesar. Chloroform (HPLC grade, \geq 99.8% purity) was obtained from Sigma-Aldrich. All chemicals were used as received.

Stock solutions of 10 mg/mL NaPSS, 5 mg/mL PFPI, and 5.0 and 7.0 M of each salt type were prepared using HPLC grade water (Sigma-Aldrich). The NaPSS stock was stirred at 70 °C for 10 min, and the PFPI stock was stirred at 85 °C for 24 h. Both stocks were then cooled to room temperature and filtered using a 0.45 μm nylon syringe filter (Fischer Scientific) before use. All salt stocks were heated to 70 °C for 10 min to ensure that salt crystals were fully dissolved. High-molarity (7.0 M KBr and 7.0 M CsBr) salt stocks were supersaturated solutions and were transferred hot for this reason, rather than being allowed to cool to room temperature before preparation of the high concentration salt samples in either series.

Samples containing 0–5.0 M LiBr, KBr, and CsBr (in 0.5 M increments) were prepared with a 50:50 molar-charge ratio of PFPI/NaPSS (1:0.6 mg/mL). The order of addition was as follows: HPLC water, salt (LiBr/KBr/CsBr), and simultaneous addition of PFPI and NaPSS. Samples were stirred at room temperature for a minimum of 8 h before any analysis was performed. Samples in photographs were allowed to separate by gravity for ~8 h before photographs were taken. Samples were centrifuged (MiniSpin Plus, Eppendorf) at 3000 rpm (252g) for 15 min in order to adequately separate the two phases for further characterization.

Samples containing PC[70]BM were prepared as follows. The dilute phase of the 3.5 M KBr solution was carefully separated from the concentrated phase. Next, 1 mL of an organic layer (either C_6H_5Cl or $CHCl_3$) containing 30 mg/mL dissolved PC[70]BM was added to the concentrated phase. The $C_6H_5Cl/PC[70]BM$ layer was found to be less dense than the aqueous concentrated phase and thus remained suspended above it, whereas the CHCl $_3$ layer containing PC[70]BM was found to be more dense than the concentrated phase and settled to the bottom of the vial (Figure S8B). These samples were then compared and characterized against the concentrated phase of a 3.5 M KBr PFPI/NaPSS standard after stirring at 650 rpm at room temperature for 2 h and again after stirring at 1150 rpm and heating to 70 °C for 43 h.

2.2. Microscopy. Images were collected with a Leica DM5500 B Widefield microscope available in the UCSC Life Sciences

Microscopy Center (Figures 1 and S1). 6 μ L of each sample was loaded onto a glass microscope slide and covered with a glass coverslip in order to arrest evaporation during imaging. Samples were excited using a 360 \pm 40 nm excitation filter and imaged with a Leica DFC450 color camera using a 20× objective and a 470 \pm 40 nm fluorescent filter.

- **2.3.** UV–Vis Spectroscopy. Dilute phase characterization was carried out for each sample after light centrifuging at 3000 rpm (252g) for 15 min. The dilute phase was carefully separated from the concentrated phase for optical density measurements taken using a Shimadzu UV-2700 spectrophotometer over the range of 300–800 nm in 1.0 nm increments in a quartz cuvette with a 1 mm pathlength (Figure S2).
- **2.4. Rheometry.** Small-amplitude oscillatory shear (SAOS) measurements were performed on the concentrated phase of each sample at the Stanford Nano Shared Facility: Soft and Hybrid Materials Facility using an ARES-G2 strain-controlled rheometer from TA Instruments in the strain-controlled oscillatory mode. A 40 mm cone-and-plate geometry with an angle of 2° and a truncation gap of 0.047 mm was used for all rheological experiments. The temperature was set at 20 °C *via* a Peltier controller, and a solvent trap was utilized to minimize evaporation of the sample during measurements.

After centrifugation and careful extraction of the concentrated phase, samples were loaded and oscillated at a low frequency and strain % (1 Hz, 5%) for 2 min prior to measurement in order to homogenize the sample. Amplitude sweeps were carried out from 0.1 to 1000% strain at an angular frequency of 31.4159 rad/s (5 Hz) in order to determine the linear viscoelastic region for each sample (Figure S4). Frequency sweeps (Figure 4 and S5) were then carried out for each sample from 0.1 to 100 rad/s and a strain % determined to fall within the linear viscoelastic region (ranging from 1 to 20 strain % depending on the sample type). All SAOS measurements were performed in triplicate to ensure the reliability of the data. Due to the inherently low viscosities of the samples, only data that fell well above the lower instrumental torque limit of 0.05 μ N·m are reported.

2.5. Time-Resolved Photoluminescence. TRPL measurements were performed via time-correlated single photon counting (TCSPC) using a home-built apparatus. Samples were excited with a pulsed supercontinuum picosecond laser (Super K EXTREME, NKT Photonics) coupled to an acousto-optic filter and an external RF driver (Super K SELECT, NKT Photonics). Measurements were carried out at a 78 MHz pulse repetition rate. The primarily horizontally polarized excitation pulse was first rotated by 90° by an achromatic $1/2 \lambda$ plate (Thorlabs) before being linearly polarized by a Glan-Thompson polarizer (Thorlabs) mounted on an automated rotation stage. Polarization of the emitted light was also varied using a Glan-Thompson polarizer. Samples were excited with vertically polarized light (400 nm), and emission was collected in a front-face geometry at a polarization of the magic angle (54.7°), with the emission wavelength centered about 440 nm. Emitted light was collimated and focused by a set of achromatic doublets (Thorlabs) onto a monochromator slit. A 420 nm long-pass filter was used to minimize any influence of the reflected excitation beam. Emission wavelengths were selected by an Acton Spectra Pro SP-2300 monochromator (Princeton Instruments). A hybrid Photomultiplier tube with minimal after-pulsing (Becker and Hickl) was used to record the time-resolved fluorescence decay. An SPC-130 photon counting module (Becker and Hickl) coupled to a Simple-Tau 130 table-top TCSPC system was used for photon counting. For magicangle measurements, collection was carried out until approximately 10,000 photon counts were reached in the main channel. After collection, magic angle data were baselined by subtracting the average of the first 30 collected data points (prior to the rise onset). Fluorescence lifetimes were determined via forward convolution with the measured instrument response function (obtained using a scattering Ludox sample) and a sum-of-exponentials model. This was carried out using the DecayFit (Fluorescence Decay Analysis Software 1.3, FluorTools, www.fluortools.com) MATLAB package developed by Dr. Soren Preus, using non-linear least squares fitting minimization. Goodness of fit was determined by the χ -squared parameter and by visual inspection of the plotted residuals.

- 2.6. Time-Resolved Photoluminescence Anisotropy. Anisotropy measurements were carried out on the setup described above. For anisotropy experiments, samples were excited with vertically polarized light (420 nm), and emission (480 nm) was collected at vertical (VV-component) and horizontal (VH-component) polarizations. Collection was carried out until approximately 20,000 counts were reached for the VH-component in the main channel. The VVcomponent measurement was then carried out for the same amount of time. Anisotropy data were time-shifted such that the max photon count of respective VV and VH signals was the same. G factor measurements were carried out in order to correct for instrumental differences in detection of the different polarization components. This was performed using horizontal excitation and collection of horizontal (HH-component) and vertical (HV-component) emission. Depolarization times were determined by fitting to two simple models simulated by Ludescher et al. 19
- 2.7. Inductively Coupled Plasma Optical Emission Spectroscopy. Li⁺, K⁺, and Cs⁺ ion concentrations of the dilute phase for each sample exhibiting phase separation were measured using a Thermo iCAP 7400 Inductively Coupled Plasma Optical Emission Spectrometer (ICP-OES). Calibration curves for each cation were established using LiBr, KBr, and CsBr standards ranging from 100 to 1000 ppm. Samples were diluted in order to reduce all salt concentrations to below the instrumental limit of 1000 ppm. Use of the ICP-OES was possible through the UCSC Earth and Marine Sciences Plasma Analytical Facility.

3. RESULTS

To prepare polyelectrolyte complex solutions, we fixed the total polymer concentration and the stoichiometric polyion charge ratio while varying the amount and type of simple salt ions. The polyanion was NaPSS, while the polycation was PFPI. The chemical structures of the polyelectrolytes are shown in Figure 1. CPEs may readily interact with salt ions via, for example, ion $-\pi$ interactions, which depend on the ion charge density and thus the ionic radius. Given the highly polarizable nature of extended π -electrons along the CPE backbone, we anticipated that the latter may also couple to the polarizability of the small ions, particularly in the high ionicstrength limit of interest to this work. Our specific choice of the salt series was made to partially ascertain the influence of cation $-\pi$ interactions on the phase behavior and optical properties of our half-CPE complex solutions. To keep this investigation tractable, we chose to use bromide salts with three alkali metal cations arranged in order of decreasing charge density and increasing polarizability: Li+, K+, and Cs+. Table 1 lists the relevant aqueous ionic radii, mean ion-water

Table 1. Characteristics of the Monovalent Cation Series 20,21,48,50,51

ion	hydration radius (Å)	charge density (\mathring{A}^{-3})	dipolar polarization $(Å^3)$	$\Delta G_{ m solv} \ m (kcal/mol)$
Li ⁺	3.82	0.54	0.032	-97.8
K^{+}	3.31	0.09	0.8 - 1.2	-54.9
Cs^+	3.29	0.05	2.4-3.1	-46.7

distance, charge densities, dipolar polarizabilities, and Gibbs free energies of aqueous solvation for the ions used in this work. 20,21,48

3.1. Phase Behavior. Figure 2 shows photographs of the aqueous polyelectrolyte complex samples before centrifugation for the three salt types after a waiting period of 24 h that allowed the solutions to settle. Visual inspection confirmed

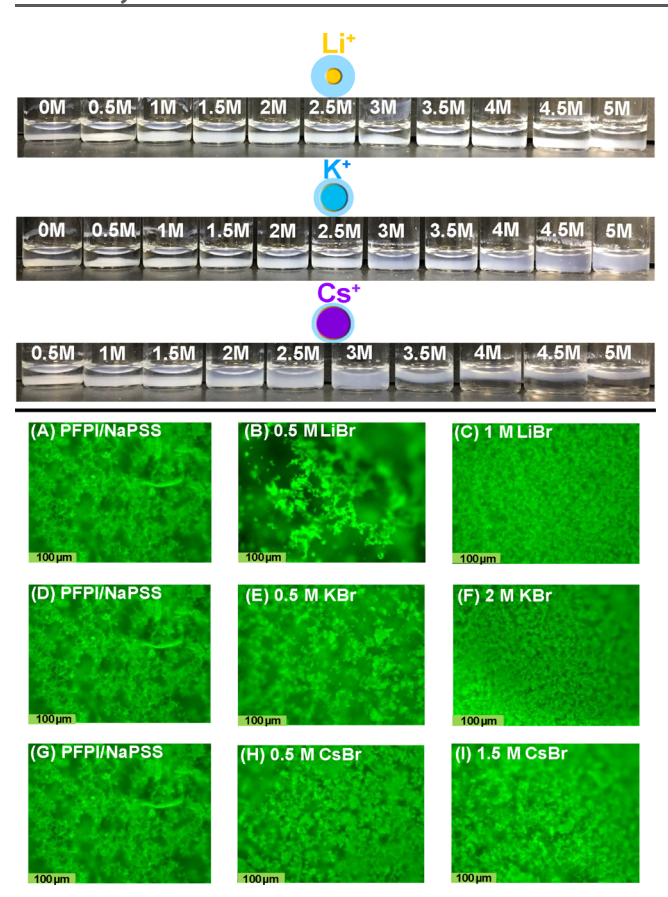


Figure 2. Top: pictures of PFPI/NaPSS complex solutions exposed to increasing LiBr, KBr, CsBr concentrations. Cartoons representing ionic and hydration radii of cations are drawn to the relative scale using values from Table 1. Bottom: fluorescent micrographs of PFPI/NaPSS complex solution with added LiBr (A–C), KBr (D–F), and CsBr (G–I) at salt concentrations before and after the nominal "solid-like" to "liquid-like" transition determined *via* rheology.

that most solutions exhibit phase separation; herein, one of the phases appears to be a dilute solution. We observe that the concentrated phase was denser than the corresponding polymer-poor supernatant for both LiBr and KBr. Surprisingly, the density of the CsBr concentrated phase appeared to be smaller than that of the supernatant at high ionic strength (<3.0 M). We used optical microscopy to ascertain whether the liquid droplet formation commonly associated with liquid—liquid phase separation was readily apparent (Figure 2A–I). We did not observe liquid droplets but rather a structure that resembled a colloidal gel with a morphology that changed with increasing salt concentration. The gel structure appears to densify as the ionic strength is increased, with the particle size gradually decreasing.

We collected similar images of samples containing PFPI at the same concentration but in the absence of NaPSS (Figure S1). Visual inspection of PFPI in the absence of NaPSS also shows phase separation, albeit with a much smaller concentrated phase. We observe a clear transition from precipitant (0.5 M of each salt) to a concentrated phase that is less opaque and exhibits lower interfacial tension between the layers at higher ionic strength. Microscopy reveals aggregate formation comparable to the low ionic strength (i.e., 0.5 M) solutions of the complex (Figure 2B,E,H). A similar phase reversal as the high ionic strength CsBr samples was seen for the concentrated phase with PFPI alone in the presence of CsBr (2.5 and 5.0 M) and KBr (5.0 M). However, in the high-salt concentration limit, the morphology of PFPI/ NaPSS differs substantially from that of PFPI alone. Whereas the former resembles a closely packed colloidal gel, the latter appears like a collection of largely small, disconnected fractal particles. Interestingly, the concentrated phase of pure PFPI samples at high [LiBr] (Figure S1C,D) are notable exceptions, with images showing what appears to be the onset of a colloidal gel.

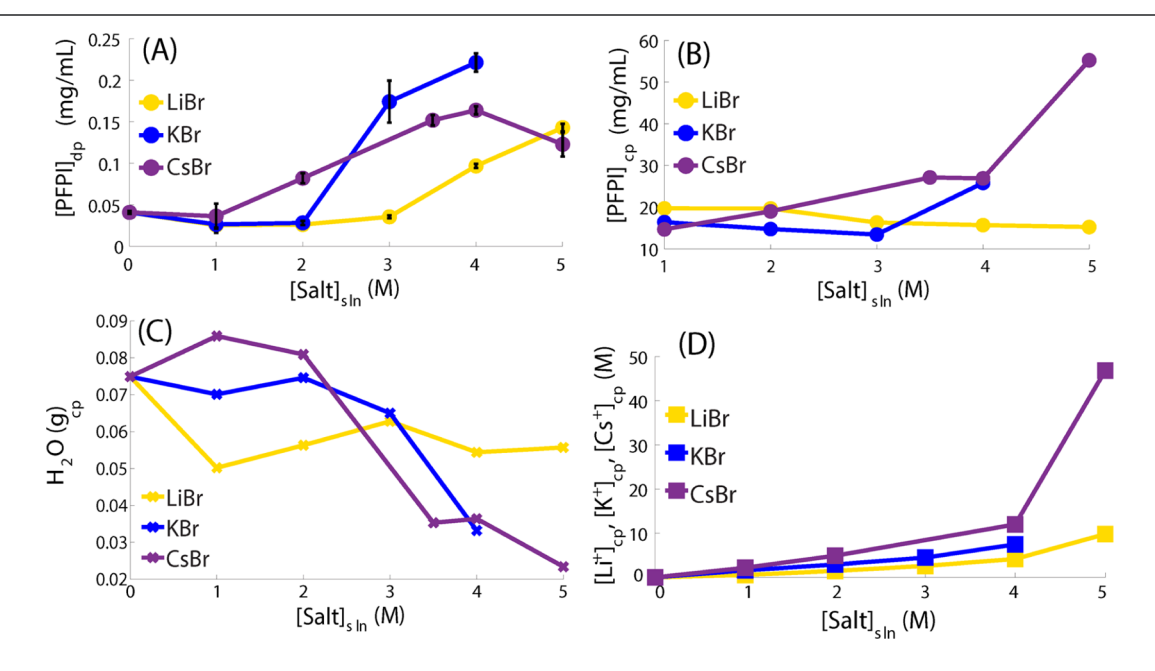


Figure 3. Phase composition. (A) Concentration of PFPI in the dilute phase ($[PFPI]_{dp}$) at each salt concentration for each salt type, as determined *via* UV–vis. (B) Concentration of PFPI in the concentrated phase ($[PFPI]_{cp}$) determined from $[PFPI]_{dp}$ and phase volumes. (C) Amount of water in the concentrated phase determined *via* lyophilization. (D) Cation concentration in the concentrated phase determined using ICP-OES dilute phase concentrations and phase volumes.

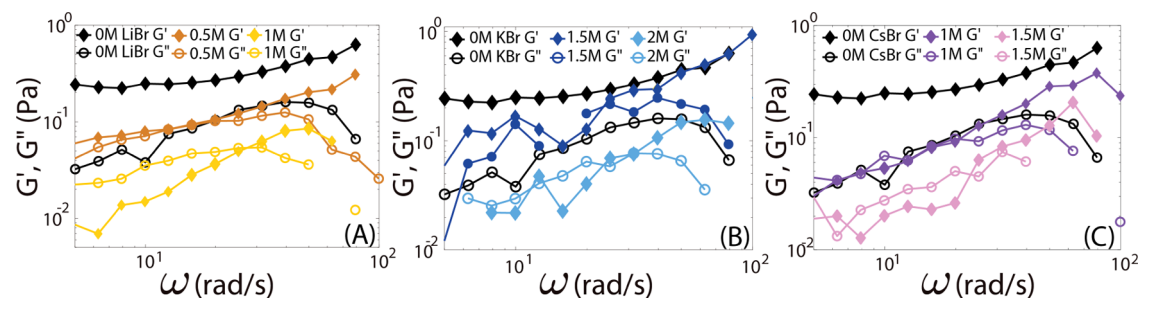


Figure 4. SOAS frequency sweeps showing select storage (G') and loss (G'') moduli for PFPI/NaPSS complexes with added (A) LiBr, (B) KBr, and (C) CsBr.

To quantify the phase separation and the partitioning of the CPE between the two phases in PFPI/NaPSS complex solutions, we first took advantage of the large extinction coefficient of PFPI to characterize the dilute phase following centrifugation. Light absorption measurements of the dilute phase of each sample indicate the presence of PFPI, which we converted to the concentration using the molar extinction coefficient of aqueous PFPI in isolation. We find an increase in the PFPI concentration with increasing salt concentration across all three salt types, as shown in Figure 3A. While this trend could generally be expected for complex coacervate-type materials, ^{7,22–24} we note that KBr leads to a larger increase in the PFPI concentration in the dilute phase relative to the other salts. For most salt concentrations, both KBr and CsBr lead to significantly more PFPI in the dilute phase relative to LiBr.

We also find a nonmonotonic ~5–10 nm spectral red shift of the PFPI absorption spectrum in the dilute phase, as well as subtle changes in the spectrum shape with increasing salt concentration (Figure S2A–C). To collectively quantify these effects, in Figure S2D we have plotted the first moment of the absorption spectrum in energy space as a function of salt concentration. This first moment decreases slightly upon addition of 0.5 M salt for all salt types, which is largely due to a red shift. For CsBr, the first moment then increases slowly but monotonically with increasing salt concentration, whereas for LiBr, the change is nonmonotonic. For KBr, the moment is largely unchanged after the initial drop and subsequent rise at 1.0 M. Together, the data imply that the ensemble of PFPI chromophores in the dilute phase depends relatively weakly on the cation nature.

Using the calculated concentration of PFPI in the dilute phase ([PFPI]_{dp}) and the estimated phase volumes following centrifugation (Table S1), the concentration of PFPI in the concentrated phase ([PFPI]_{cp}) of each sample was determined. Figure 3B shows that [PFPI]_{cp} $\sim 20~\text{mg/mL}$ at [LiBr] = 1 M, and [PFPI]_{cp} is comparable for all three salts up to 2.0 M. [PFPI]_{cp} decreases slightly as [LiBr] is increased past 1 M, while [PFPI]_{cp} undergoes a substantial increase with increasing [KBr] and [CsBr] over the same salt concentration range. Interestingly, [PFPI]_{cp} in all cases is well above 10 mg/mL, which is the concentration at which pure PFPI forms a hydrogel in an aqueous solution with no excess salt.

Further phase composition analysis was carried out to determine the water and cation content. Using gravimetric analysis and lyophilization, we estimate that the water content in the concentrated phase is relatively small. Using our estimated phase volumes, we find a water concentration in the range of 3–6 M. Figure 3C shows that the water mass decreases with increasing ionic strength. This suggests that as

more salt is available in solution, more ions enter the complex and displace water. This is supported by the cation concentration increase in the concentrated phase, as shown in Figure 3D. These values were obtained using the dilute phase ion concentration *via* ICP-OES analysis (Figure S3B) and phase volumes (Table S1). The particularly large [PFPI]_{cp} and Cs⁺ concentration in the concentrated phase at 5 M total [CsBr] is a direct consequence of the drop in phase volume.

3.2. Rheology. Having characterized the PFPI composition of the dilute phase, the nature of the concentrated phase was then interrogated. The question to be answered is, can a π -CPE complex coacervate be formed using salt-induced phase separation in aqueous solution? Here, we turned to rheology to characterize the viscoelastic properties of the concentrated phase of each sample. Specifically, we preformed SAOS measurements, in which a specified sinusoidal strain is applied at an angular frequency (ω) , and the resultant stress is measured. Phase-separated samples were centrifuged before carefully extracting the concentrated phase prior to measurements

The mechanical response of a viscoelastic material is conveniently described in terms of the complex frequency-dependent modulus. The time-dependent ratio of the applied stress (σ) to the material strain (γ) in a SAOS measurement is given by a combination of an in-phase and an out-of-phase component as

$$\frac{\sigma(\omega, t)}{\gamma} = G' \sin(\omega t) + G'' \cos(\omega t) \tag{1}$$

This expression includes the real part of the complex modulus, or the elastic modulus (G'), which is related to the stored elastic energy upon deformation. The purely imaginary loss modulus (G'') describes energy dissipation. Under sinusoidal shear, the dissipative term lags the elastic term by a phase angle δ , the (loss) tangent of which is given by

$$\tan(\delta) = \frac{G''}{G'} \tag{2}$$

A $\tan(\delta)$ < 1 is indicative of a primarily solid-like, elastic response where G' dominates over G'', whereas the opposite is true for samples with predominantly viscous, liquid-like response. Figure 4A–C shows the storage and loss moduli at select ion concentrations as a function of ω in the presence of LiBr, KBr, and CsBr, respectively.

The frequency sweep data show a trend of decreasing modulus with increasing salt concentration, as is expected for polyelectrolyte complex materials (Figure 4). $^{24-28}$ The viscoelastic response of the complexes prepared in the absence of added salt is dominated by G' over the entire range of

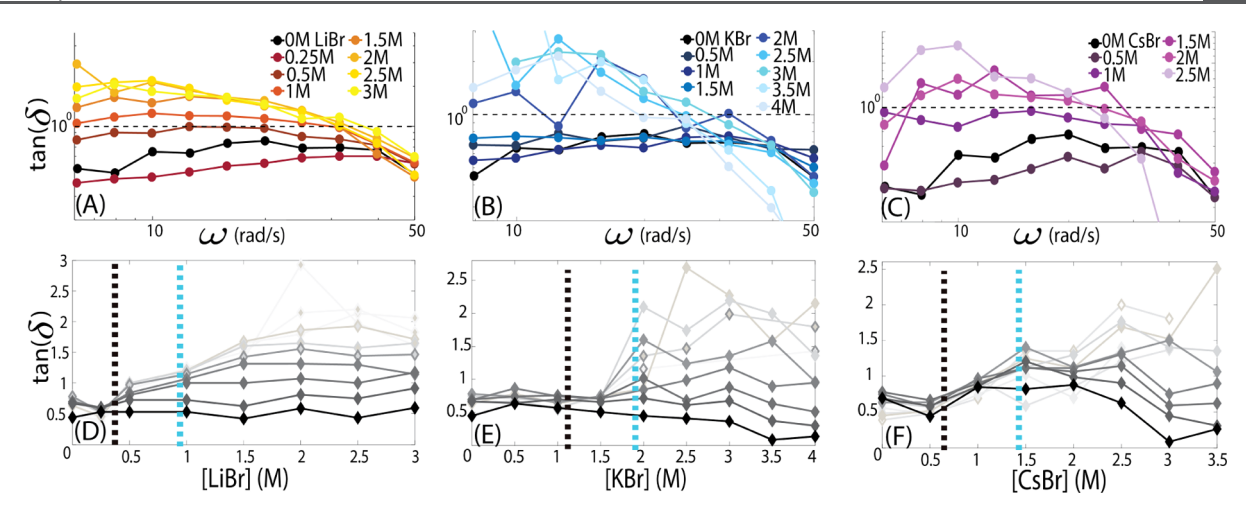


Figure 5. Frequency sweep results. $Tan(\delta)$ vs frequency (5-50 rad/s) for PFPI/NaPSS complexes with added (A) LiBr, (B) KBr, and (C) CsBr. $Tan(\delta)$ vs [salt] [gray scale represents frequency range: 5 (light-gray)-50 (black) rad/s] for (D) LiBr series, (E) KBr series, and (F) CsBr series where solid-like (left of dotted black line), gel-like (left of dotted blue line), and liquid-like (right of dotted blue line) regions are highlighted.

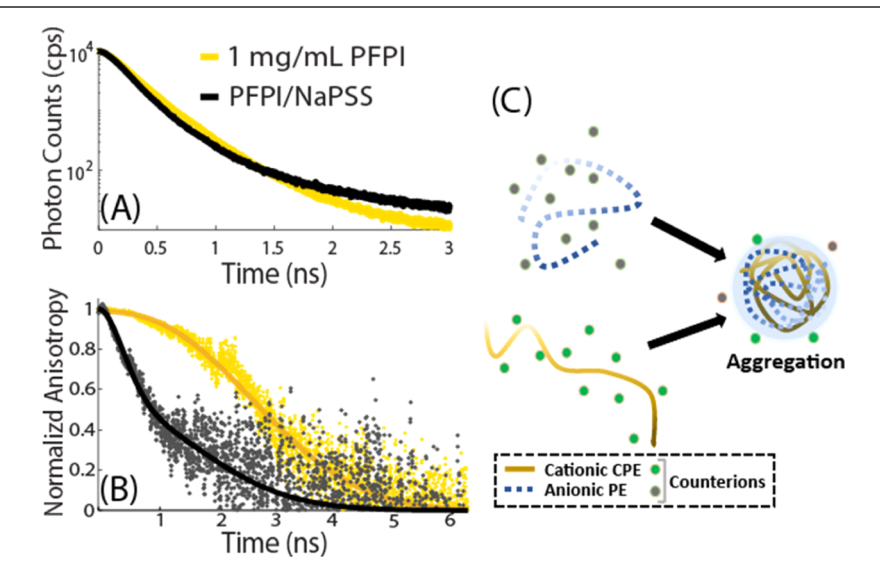


Figure 6. Time-resolved spectroscopy. (A) TRPL and (B) TRPL anisotropy comparing a dilute solution of PFPI (1 mg/mL) to complexes of PFPI/NaPSS (1:0.6 mg/mL) with no added salt. (C) Complexation cartoon, showing tight coiling of PFPI, which leads to rapid exciton hopping and thus a fast PL depolarization decay time.

frequencies sampled, indicating that it behaves largely as an elastic solid. However, with increasing salt concentration, we observe a change in the viscoelastic response, with samples prepared at higher salt concentrations showing behavior that is dominated by G'' at low frequency and G' at higher frequency. These trends can also be observed by plotting the loss tangent as a function of ω (Figure 5A–C), with more viscous, liquidlike behavior emerging at salt concentrations around 1.0 M LiBr, 2.0 M KBr, and 1.5 M CsBr. It is worth mentioning that the low viscosity of the high-ionic strength samples (i.e., 2.0-3.0 M KBr and 1.5-3.5 M CsBr) introduced more noise in low-frequency measurements as the measured stress approaches the instrumental limit. This suggests that the strength and/or number of interaction regions in the complex decreases with increasing ionic strength, likely due to the large increase in the ion content of the complex that can compete with the electrostatic interactions between the polyelectrolytes themselves. Overall, the viscoelastic response of these materials appears similar to that of a polymer melt or colloidal gel, which

has been reported previously for a range of polymeric complex coacervates. $^{24-26,28}$

While the trends in the frequency-dependent viscoelastic response are similar to those reported for other polyelectrolyte complex materials, it is worth noting the extremely low magnitude of the modulus overall. For example, the modulus of solid-like NaPSS in complex with poly-(diallyldimethylammonium chloride) in the presence of low concentrations of KBr was in the range of 10⁴ to 10⁵ Pa. However, for PFPI/NaPSS complexes, the highest value of the modulus is on the order of 1 Pa. This dramatic difference in the modulus could be explained by the low water content and the colloidal gel-like morphology of the complex solution.

Defining the liquid- or solid-like character of a viscoelastic material can be challenging as this response is generally a function of frequency. However, polyelectrolyte complex coacervates have been shown to undergo salt-dependent solidification that can be described as physical gelation. The critical gel point can be identified based on the presence of a frequency invariant response in the material. This

transition can be more clearly observed by plotting the loss tangent as a function of salt concentrations at different ω (Figure 5D-F). We break down the response of the material into three regions. As shown in Figure 5D-F, the area left of the black dotted line on each plot roughly corresponds to salt concentrations which exhibit a solid-like material response. Interestingly, the addition of salt does not appear to have a significant effect on the loss tangent of the solid material, which is different from previous reports.²⁴ The area between the black and blue dotted lines corresponds to the region where a solid-to-liquid transition occurs, and the area right of the blue dotted line corresponds to concentrations which exhibit a more viscous, liquid-like response. The regions which show evidence of a liquid-like response for each salt type were found to be as follows: 1.0-5.0 M for LiBr; 2.0-4.0 M for KBr; and 1.5-5.0 M for CsBr, excluding 3.0 M CsBr, for which no phase separation was observed on the timescale between sample preparation and measurements, or upon centrifugation. These data provide evidence for the salt-driven formation of a liquid CPE complex coacervate phase, albeit one that appears to differ from a classical coacervate phase in its morphology.

3.3. Time-Resolved Photoluminescence with No Excess Salt. Having characterized the rheological properties of the concentrated phase, we studied whether increasing salt concentration had an influence on the photophysical properties of the CPE within the concentrated phase. The delocalized electronic states of a CPE are sensitive to the microstructure of the chain, which leads to photophysical properties that closely track the ensemble of chain conformations. Thus, spectroscopic techniques can be used to probe the structure of the complexes without the need for secondary reporters. TRPL is a convenient and informative spectroscopic probe because it is highly sensitive to intra- and inter-chain excited-state delocalization. Different TRPL decay components can, in principle, be related to radiative relaxation due to different microstructural states or environments.

Figure 6A shows the TRPL decay from both isolated aqueous PFPI solution with no excess salt and the concentrated phase of the PFPI/NaPSS complex solution, similarly with no added salt. We used a front-face geometry to collect TRPL measurements on concentrated samples following centrifugation. All decays were successfully deconvolved from the instrument response function using a biexponential model, which was the minimal model necessary to capture the functional form of the decays. The lifetimes from deconvolved decays are listed in Table 2. Pure PFPI shows a distinct biexponential decay with short (150 ps) and long (360 ps) lifetime components. Upon addition of NaPSS, there is a subtle increase in the short component (230 ps) accompanied by a significant increase in the long component (1.08 ns). This suggests a shift in the photophysical properties of PFPI due to a change in the microstructure of the conjugated backbone upon complexation (Figure 6C).

Additional insights into the change in CPE microstructure upon complexation can be obtained by performing a polarization-sensitive time-resolved PL anisotropy measurement. In this experiment, the sample is excited with a vertically polarized light pulse, and the time-resolved fractional difference between emission parallel and perpendicular to the excitation is tracked. If the ensemble—average transition dipole moment of the emitting state changes orientation with time, emission will become depolarized, acquiring a horizontal

Table 2. Deconvolved PL Lifetimes and Component Amplitudes

1					
sample	a_1	$\tau_1 \; (\mathrm{ns})$	a_2	τ_2 (ns)	$\langle \tau \rangle$ (ns)
1 mg/mL PFPI	0.997	0.15	0.003	0.36	0.15
PFPI/NaPSS	0.999	0.23	0.001	1.08	0.23
0.5 M LiBr	0.999	0.26	0.001	1.25	0.26
1.0 M LiBr	0.999	0.26	0.001	1.18	0.26
1.5 M LiBr	0.999	0.23	0.001	1.13	0.24
2.0 M LiBr	0.999	0.24	0.001	1.20	0.25
2.5 M LiBr	0.999	0.25	0.001	1.15	0.25
3.0 M LiBr	0.999	0.21	0.001	1.26	0.21
3.5 M LiBr	0.999	0.22	0.001	1.15	0.22
4.0 M LiBr	0.999	0.23	0.001	1.20	0.23
4.5 M LiBr	0.999	0.22	0.001	1.12	0.22
5.0 M LiBr	0.998	0.26	0.002	1.13	0.27
0.5 M KBr	0.995	0.29	0.005	1.04	0.30
1.0 M KBr	0.992	0.34	0.008	1.12	0.36
1.5 M KBr	0.991	0.34	0.009	1.10	0.36
2.0 M KBr	0.987	0.36	0.013	1.08	0.38
2.5 M KBr	0.989	0.35	0.012	1.10	0.38
3.0 M KBr	0.987	0.35	0.013	1.07	0.38
3.5 M KBr	0.979	0.40	0.021	1.12	0.44
4.0 M KBr	0.991	0.33	0.009	1.08	0.35
4.5 M KBr	0.987	0.35	0.013	1.08	0.38
5.0 M KBr	0.990	0.34	0.010	1.08	0.36
0.5 M CsBr	0.997	0.28	0.003	1.10	0.28
1.0 M CsBr	0.998	0.28	0.003	1.16	0.29
1.5 M CsBr	0.996	0.29	0.004	1.14	0.31
2.0 M CsBr	0.995	0.32	0.005	1.19	0.33
2.5 M CsBr	0.996	0.30	0.004	1.17	0.31
3.0 M CsBr	0.995	0.32	0.005	1.14	0.33
3.5 M CsBr	0.992	0.34	0.008	1.14	0.36
4.0 M CsBr	0.990	0.34	0.010	1.13	0.37
4.5 M CsBr	0.992	0.34	0.009	1.10	0.36
5.0 M CsBr	0.991	0.34	0.009	1.11	0.37

component. Thus, this technique is sensitive to exciton migration and physical motion of CPE chains.

The normalized PL anisotropy dynamics for the isolated PFPI solution and the concentrated phase of the salt-free PFPI/NaPSS complex are shown in Figure 6B. The anisotropy of PFPI in isolated aqueous solution depends weakly on time over a period longer than the average PL lifetime. This indicates that the PFPI backbone contains regions that are significantly extended. An extended chain with a limited number of inter-chain interactions has few ways to scramble the orientation of the transition dipole moment of the emitting exciton state. At longer times, rotation of chromophores along the chain or overall chain rotation will nevertheless depolarize the emission, which leads to a complete decay of the anisotropy. Comparing the normalized anisotropy of pure PFPI to that of the concentrated phase of the salt-free complex solution shows that the rate of depolarization is increased significantly upon complexation with NaPSS. Such an observation is consistent with significantly more collapsed chains within the complex as this allows for facile exciton hopping between chromophores either along the same chain or between different chains. This scrambles the memory of the initial orientation of the average transition dipole moment and thus leads to anisotropy decay.

3.4. Time-Resolved Photoluminescence with Excess Salt. Figure 7A–C shows TRPL decays of the concentrated

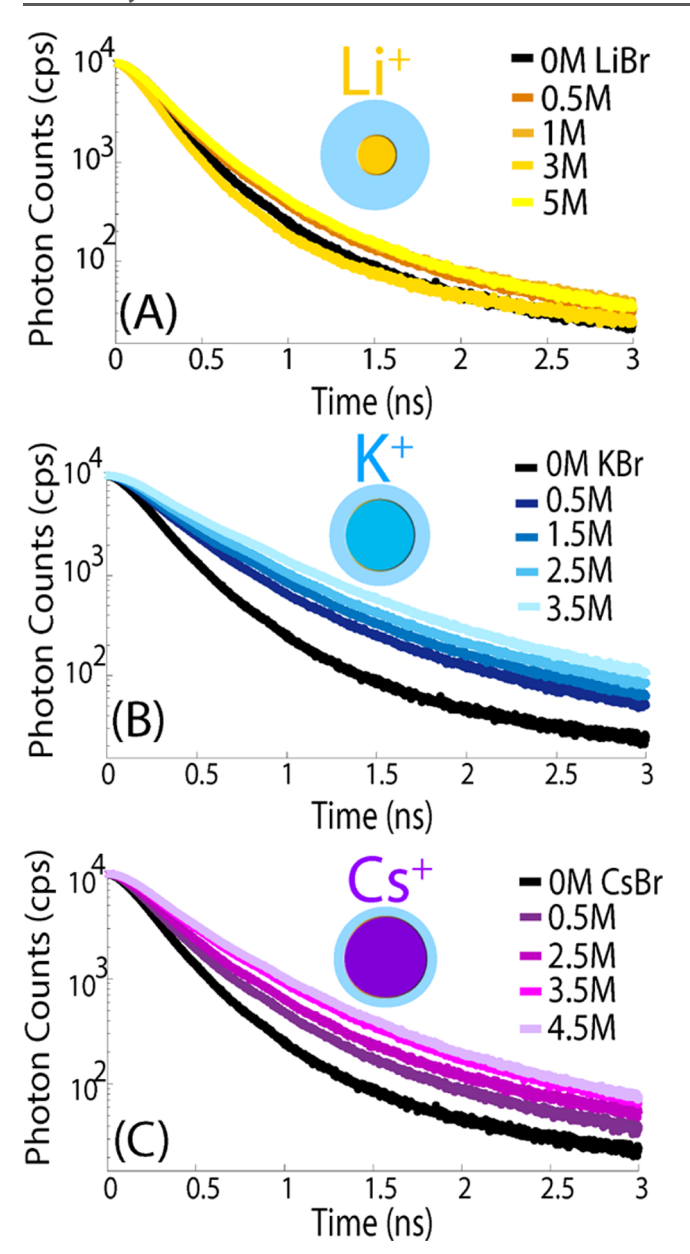


Figure 7. TRPL decay curves of the concentrated phase upon increasing (A) LiBr, (B) KBr, and (C) CsBr.

phase for select salt concentrations, which capture the observed trend for each salt type. Table 2 lists the deconvolved lifetimes and their amplitude for the concentrated phase. Table 3 shows the comparison between the concentrated-phase PFPI lifetime with the corresponding dilute phase at select salt concentrations. Upon exposure of the complex to increasing

Table 3. Average PL Lifetime Comparison for Diluted and Concentrated Phases

diluted phase	$\langle \tau \rangle$ (ns)	concentrated phase	$\langle \tau \rangle$ (ns)
2 M LiBr	0.16	2 M LiBr	0.25
4 M LiBr	0.21	4 M LiBr	0.23
2 M KBr	0.22	2 M KBr	0.38
4 M KBr	0.27	4 M KBr	0.35
2 M CsBr	0.22	2 M CsBr	0.33
4 M CsBr	0.26	4 M CsBr	0.37

LiBr (Figure 7A), we observe little variation in emission dynamics, which are dominated by the short lifetime component. The average PFPI lifetime for the LiBr series was found to fluctuate around ~241 ps. An intriguing difference is seen upon exposing the complex to increasing KBr. We find a monotonic increase in the average PL lifetime, which corresponds to an approximately 50% increase at 3.5 M KBr compared to the complex on its own (230 ps vs 440 ps). Increasing CsBr gives qualitatively similar results to KBr. In the high-salt concentration limit, the concentrated phases of both KBr and CsBr also show similar PL lifetimes. This suggests that, on average, PFPI chains within the complex adopt a similar microstructure, a result that is in agreement with trends from rheology. A comparison of lifetimes collected for the concentrated phase of PFPI in the absence of NaPSS at select LiBr, KBr, and CsBr concentrations can be found in Table S2. Although increasing ionic strength does lead to an increase in the PL lifetime in the concentrated phase of PFPI on its own, the PFPI lifetime in the concentrated phase of PFPI/NaPSS is larger than PFPI alone for most samples. We observe the largest relative increase for KBr, with the PFPI/NaPSS complex having a lifetime that is 46% longer than the corresponding concentrated phase without NaPSS.

To better compare the change in PL lifetime with salt concentration for each salt type, Figure 8A shows plots of the short and long lifetime components, respectively, as a function of salt concentration for the three salts. Figure 8C shows the fractional contribution of the short component, $F_1 = a_1 \tau_1 / (a_1 \tau_1)$ $+ a_2 \tau_2$), where a_1 is the amplitude of the short component, a_2 is the amplitude of the long component, τ_1 is the lifetime of the short component, and τ_2 is the lifetime of the long component. The short component for LiBr shows no obvious trend with increasing salt concentration, with the lifetime remaining largely unchanged compared to the salt-free complex. In contrast, increasing both KBr and CsBr leads to a monotonic increase in the short component. It is interesting to note that the rate at which this lifetime evidently reaches saturation at high salt is larger for KBr than for CsBr, suggesting a more gradual change in the PFPI chain microstructure for CsBr. Relatively minor but readily measurable changes in F_1 are found to accompany changes in emission lifetimes. Figure 8B shows that most of the exciton population emits over the short decay lifetime. Upon increasing KBr and CsBr, a small decrease is observed in the short component fraction with increasing ionic strength. Interestingly, we observe no significant changes in the long component lifetime, which fluctuates about \sim 1.1 ns regardless of simple salt type.

It is well known that conjugated polymers can support excitons that are delocalized over a single chain or shared between two or more chromophores located either along a single coiled chain or between proximal chains. When excitons are largely delocalized along the CPE backbone, the PL lifetime is expected to be relatively long, corresponding to J-like excitons. ^{29,30,40–43} In contrast, when the exciton center-of-mass wavefunction is shared between multiple chromophores, the PL lifetime becomes relatively small, which corresponds to H-like excitons. With this simplified model in mind, we interpret the short PFPI lifetime component in the concentrated phase as arising from regions with substantial inter-chromophore (monomer—monomer) interactions. The long component should then be associated with PFPI chains with relatively few inter-chromophore interactions.

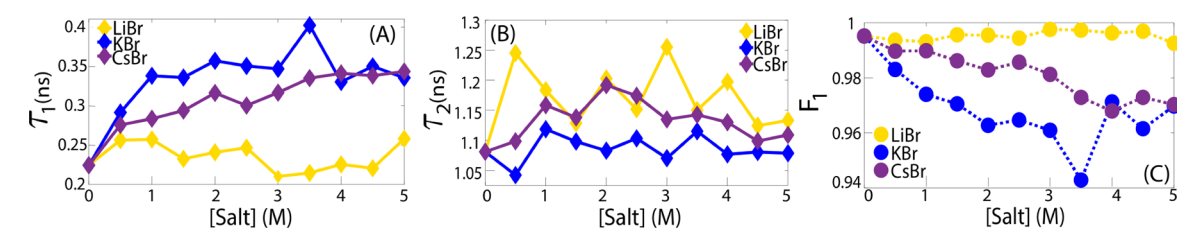


Figure 8. PL lifetimes and decay component amplitudes in the concentrated phase as a function of salt concentration. (A) Short and (B) long lifetimes (τ_1 and τ_2 , respectively) vs [Salt] for each salt type. (C) Factional contribution to the short decay lifetime vs [Salt] for each salt type.

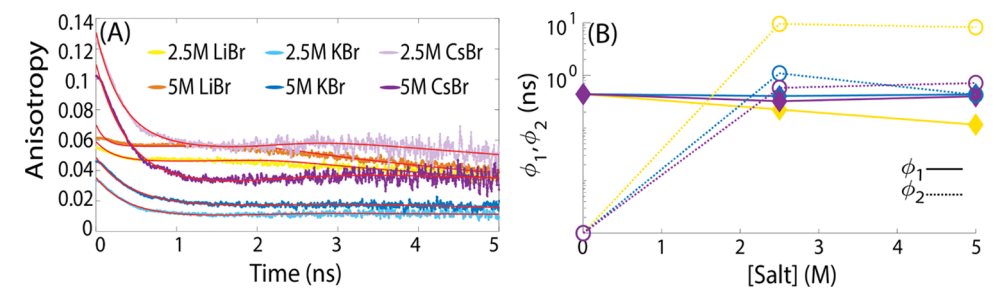


Figure 9. PL depolarization dynamics in the concentrated phase. (A) Time-resolved PL anisotropy decays of PFPI/NaPSS with 2.5 M and 5.0 M LiBr (yellow), KBr (blue), and CsBr (purple) where red lines indicate fits. (B) Fast (φ_1 , solid lines with diamond markers) and slow (φ_2 , dotted lined with open circle markers) correlation times vs [Salt] for PFPI/NaPSS complexes with 2.5 and 5.0 M LiBr, KBr, and CsBr.

ı

3.5. Salt-Dependent PL Anisotropy Dynamics. We performed time-resolved PL anisotropy measurements on the concentrated phase at select salt concentrations for each salt type within the region that showed rheological evidence for the formation of liquid coacervate-like states (2.5 and 5.0 M LiBr, KBr, and CsBr). We found that transferring the concentrated phase into the optical cuvette resulted in a slow change of the measured anisotropy over the first ~5 h of the sample resettling. For this reason, results shown below are from samples that were allowed to mechanically settle for a minimum of 24 h before measurements were taken. Additional decays collected immediately upon transfer to the cuvette and 5 h after loading of the cuvette can be found in Figure S10 and Table S4. We find that all anisotropy curves at the abovementioned salt concentrations display a fast-initial decay. However, the anisotropy does not decay to zero on the timescale of the experiment, and for certain samples, the shape of the anisotropy decay at intermediate times is complex, displaying a local maximum.

Such nontraditional anisotropy decay shapes have previously been reported in the biophysical literature, where timeresolved anisotropy had been used to probe small-molecule fluorophores either free in solution or bound to large particles such as proteins or membranes.³¹ In a system which contains a population of both bound and unbound fluorophores, that is, one that displays spatial heterogeneity, the anisotropy can increase in time instead of monotonically decaying to zero. 19,31,32 In such systems, the decay rate of PL depolarization had previously been attributed to the rotational motion of the fluorophore. Such complex anisotropy behavior has also been observed in time-resolved vibrational anisotropy experiments on water in inverse micelles with interfacial and bulk-like liquid states.³³ Analogous interpretation in the case of conjugated polymers in condensed phases is more complicated. This is because PL can be depolarized both by exciton hopping via electronic energy transfer between chromophores and by rotational motion of the chain.

To extract quantitative information, we have applied two simple physically motivated models. These models were previously simulated by Ludescher et al. to elucidate how differences in PL lifetime components coupled with spatial heterogeneity influence the observed time-resolved anisotropy decay curves. 19 Modeling anisotropy decays allows us to extract PL depolarization times. These can then be compared to gain insights into the differences in local environments experienced by the CPE chain in the presence of different salts. In both models, the short and long PL lifetime components (Figure 8A,B) are associated with their own distinct anisotropy decay laws. In model 1, for a given PL lifetime component, the anisotropy decay comprises two terms, the first of which is a single exponential and the second is a constant. The constant term accounts for the fact that in relatively large macromolecular assemblies, the anisotropy may not decay to zero on the timescale of the experiment. The anisotropy, r(t), then takes the following functional form

$$\begin{split} r(t) &\propto f_1(t) \Bigg[\alpha_1 \mathrm{exp} \Bigg(-\frac{t}{\varphi_1} \Bigg) + (1 - \alpha_1) \Bigg] \\ &+ f_2(t) \Bigg[\alpha_2 \mathrm{exp} \Bigg(-\frac{t}{\varphi_2} \Bigg) + (1 - \alpha_2) \Bigg] \end{split} \tag{4}$$

where α_i is the fraction of the anisotropy decay with depolarization time φ_i , associated with given lifetime component $(a_v\tau_i)$. Here, φ_1 is associated with the shorter PL lifetime (τ_1) , while φ_2 is associated with the longer lifetime (τ_2) . The α_i were not constrained to sum to unity to allow for a relative difference in the fundamental anisotropies (*i.e.*, limiting anisotropy as time goes to zero) of the two components. The time-dependent weights $f_i(t)$ that determine the contribution of each anisotropy decay law in square brackets are constrained by the fractional PL lifetime decay (describing the time dependence of the exciton population) as

$$f_i(t) = a_i \exp\left(-\frac{t}{\tau_i}\right) / \sum_{j=1}^2 a_j \exp\left(-\frac{t}{\tau_j}\right)$$
(5)

where τ_i is the PL lifetime and a_i is the amplitude of the excited-state population characterized by that lifetime (Table 2). The time dependence of the f_i gives rise to the complexity of the anisotropy decay form.

When model 1 was insufficient to capture the functional form of the anisotropy satisfactorily, we used a slightly modified model. Model 2 differs from model 1 via an additional multiplicative term, which describes the timescale for the overall depolarization of a generalized "large particle", $\varphi_{\rm p}$, to which sub-populations with φ_1 and φ_2 are bound

$$r(t) \propto \left\{ f_1(t) \left[\alpha_1 \exp\left(-\frac{t}{\varphi_1}\right) + (1 - \alpha_1) \right] + f_2(t) \left[\alpha_2 \exp\left(-\frac{t}{\varphi_2}\right) + (1 - \alpha_2) \right] \right\} \exp\left(-\frac{t}{\varphi_p}\right)$$
(6)

Solid red lines in Figure 9A indicate fits to the above models. Although the models are simple given the complexity of our system, they do a reasonably good job of qualitatively capturing the entirety of the data set. Nevertheless, the fits are not perfect and some caution is warranted in interpretation.

Anisotropy fitting parameters are listed in Table 4. Figure 9B shows a plot of φ_1 and φ_2 for two concentrations from each

Table 4. Time-Resolved PL Anisotropy Fitting Parameters

sample	φ_1 (ns)	α_1	φ_2 (ns)	α_2	$\varphi_{\rm p}$ (ns)
PFPI/NaPSS (t _{24 hrs})	0.44	0.77	0.001	0.50	
2.5 M LiBr (t _{24 hrs})	0.22	0.22	9.45	1.00	
5.0 M LiBr (t _{24 hrs})	0.12	0.21	8.21	1.00	
$2.5~M~KBr~(t_{24~hrs})$	0.40	0.76	1.09	0.69	
5.0 M KBr (t _{24 hrs})	0.44	0.63	0.43	0.52	12.6
$2.5~M~CsBr~(t_{24~hrs})$	0.32	0.55	0.58	0.43	12.4
$5.0 \text{ M CsBr } (t_{24 \text{ hrs}})$	0.40	0.71	0.56	0.60	22.4

salt type. For the complex with no excess salt, the primary contribution to the anisotropy decay comes from $\varphi_1 \sim 0.44$ ns. A similar φ_1 is found for samples in the presence of both KBr and CsBr, whereas it is nominally smaller for LiBr by nearly a factor of 2 (<0.23 ns), though the fits at short time for LiBr are noticeably worse. Evidently, adding salt introduces a significant contribution from an additional depolarization time φ_2 which falls between ~0.4 and ~1 ns for KBr and CsBr depending on the sample. Interestingly, φ_2 is significantly larger for LiBr (~9 ns).

4. DISCUSSION

In this work, we first set out to characterize the nature of aqueous phase separation in oppositely charged complexes containing a CPE. Second, we aimed to determine what the influence of phase separation was on the photophysical properties of the CPE, if any, both within the dilute and concentrated phases. Our final objective was to uncover whether the nature of the monovalent cation influenced the phase behavior and the photophysical properties of our system.

Using rheological measurements, we found evidence for the formation of a viscoelastic liquid coacervate phase for all three

simple bromide salts that were investigated. However, microscopy measurements showed that PFPI/NaPSS samples resembled a colloidal gel whose morphology changed with increasing salt concentration. Thus, although rheological measurements suggest the formation of a viscoelastic liquid phase, we believe the phase behavior is more complex. Danielsen et al. found that in water/THF mixtures at a certain solvent mixture composition, the phase behavior was indicative of what they referred to as coacervate-precipitates. 15 Based on our observations, we believe it is likely that the concentrated phase in our samples also exhibits a coexistence of liquid-like and solid-like domains, which give rise to the colloidal gel-like microstructure. The salt concentration at which liquid-like behavior was observed was higher than what was previously observed with non-conjugated polyelectrolyte complexes. We speculate that such phase behavior is related to increased hydrophobic and/or monomer-monomer interactions of CPEs compared to most non-conjugated polyelectrolytes.

Our supposition that the microstructure of the concentrated phase resembles a colloidal gel is consistent with the observation of two PL lifetime components, suggesting two distinct local environments: a primary sub-population associated with the short PL lifetime and a minor one associated with the long lifetime. Previous work on simulations of colloidal gels showed that such a system is likely to be dynamically heterogeneous, displaying particle populations with two distinct relaxation times (slow and fast).⁴⁹ We propose that the short PL component is associated with relatively closely packed "slow" particles with substantial interchromophore PFPI interactions. Exciton hopping between chromophores within these populations ought to be relatively rapid, potentially leading to the short anisotropy depolarization time. The longer PL lifetime should then be associated with a minor population of "fast" gel particles, where PFPI chains exist in a relatively extended conformation and perhaps form connecting tie-chains between the slower particles. The long depolarization time of such particles would be consistent with the relatively large chain extension, leading to intrachain exciton delocalization and a relatively long memory of the initial transition dipole moment orientation. A cartoon of such a coexistence is shown in Figure 10. The PL lifetime of PFPI in the dilute solution (Table 3) was smaller than that of PFPI within the complex and effectively possessed only one decay component. It is clear that the local environment experienced by PFPI is qualitatively different in the two phases, presumably with more intra-chain π -stacking interactions between isolated chains occurring in the dilute phase.

It is interesting that the PFPI PL lifetimes within the concentrated phase changed markedly with increasing KBr and CsBr but remained relatively unchanged with LiBr. This is despite the fact that, based on the rheological characterization, differences between the concentrated phases at a given salt concentration across the salt series were not drastic. Although the role of the bromide anion cannot be ignored, we focus on the cation $-\pi$ interaction under the simplifying assumption that anion-induced interactions are approximately unchanged as the cation varied. ^{34,35}

The cation– π interaction will contain contributions from the screened Coulomb interactions of the ion primarily with the quadrupole moment of the aromatic CPE backbone, as well as the coupling between the polarizability of the ion and π -electrons. The Li⁺ charge density is largest across the cation series, which leads to the strongest Coulombic cation– π

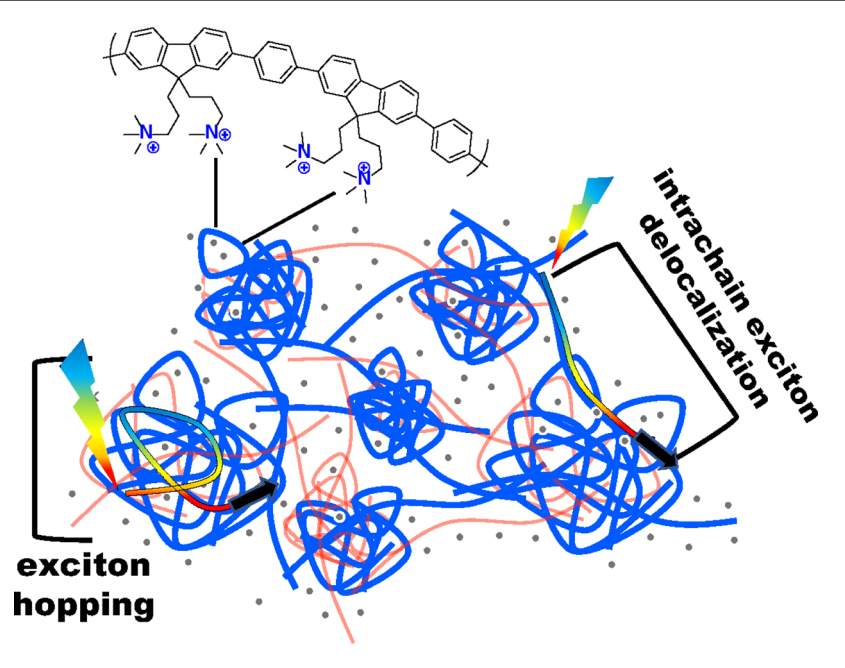


Figure 10. Cartoon showing a coexistence between domains within the colloidal gel where the chain is coiled and excitons hop rapidly between chromophores, as well as regions where the chain is relatively extended.

interaction in the gas phase compared to K⁺ and Cs⁺. However, the cation $-\pi$ interaction is significantly modified by hydration of both the ion and the aromatic backbone in the aqueous medium, resulting in substantial differences in desolvation free energy (Table 1). In fact, motivated by understanding biological ion-conducting channels, prior work has shown that the strength of the cation $-\pi$ interaction can undergo a relative reversal compared to its gas-phase value.³⁷ Relative to Li^+ , it was observed that the aqueous cation $-\pi$ interaction with K+ could be stronger and could be competitive with the water-K+ interaction. This reversal from the gas phase to the aqueous phase was largely attributed to the larger desolvation penalty for Li⁺ relative to K⁺. ^{20,38} Measurements of the cation concentration in the dilute phase indicate that the dilute phase in the presence of LiBr has a slightly larger Li⁺ concentration (Figure S3B) compared to the other cations, which is consistent with the larger desolvation cost. There is further evidence from vibrational predissociation spectroscopy that K⁺ may act as a bridge between aromatic regions.³⁹

Recent molecular dynamics simulations have shed substantial light on the nature of the cation- π interaction at extended aromatic surfaces of relevance to this work. Simulations by Pham et al. using first-principles calculations of aqueous carbon nanotube-ion interactions show that K+ has a larger binding energy with the nanotube surface than either Na⁺ or Cl^{-.52} This leads to preferential K⁺ adsorption at the aromatic surface relative to the middle of the tube. The reasons for this were (i) significant nanotube-ion wavefunction hybridization and (ii) a "softer" solvation shell with significant water reorganization. These factors result in the K⁺ becoming partially desolvated when near the surface. In contrast, the Na⁺ ion remained fully solvated and displayed substantially less wavefunction hybridization with the carbon nanotube. These authors used a 1 M ion concentration commensurate with this work. It is also intriguing that the authors do not find a static K+-nanotube interaction. Instead, it is seen that K+ readily diffuses along the nanotube surface. Additionally, Williams et al. used parameterized polarizable

force fields to study graphene—ion interactions and converged on a similar result: aqueous K^+ interacts quite strongly with graphene. The first (global) minimum of the potential of mean force was larger than that of Li^+ , once again showing partial dehydration of K^+ at the graphene surface. In contrast, Li^+ retained its hydration shell even in proximity of the extended aromatic surface. It is worth noting that there was some disagreement between the two studies regarding the degree of Na^+ dehydration. This was attributed to differences in the curvature of the aromatic surface.

In addition to differences in desolvation free energies, the dipolar polarizability increases by a factor of ~31 from Li⁺ to K^+ and by ~ 2.75 in going from K^+ to Cs^+ . The difference between K+ and Cs+ is significant, yet the relative photophysical changes seen as a function of salt concentration are similar. However, it is notable that the concentrated phase at high ionic strength appears to be significantly more enriched in Cs+ than K+ and Li+. We believe the increase in the Cs+ polarizability leads to a stronger interaction with the conjugated CPE backbone and thus a better "solvation" environment for the CPE backbone in the concentrated phase compared to the other cations, particularly when the water content is low. Interestingly, we found that K+ led to a faster jump in PL lifetime with increasing salt concentration compared to Cs+, although the two ions converge on the same lifetime at the highest concentrations. Motivated by the work of Pham et al., we speculate that this may be due to a larger K+ diffusion coefficient along the aromatic surface compared to Cs⁺. ⁵² Thus, more Cs⁺ may be required to observe the same overall influence on the CPE backbone. This possibility raises intriguing questions about how one might vary the nature of the cation to manipulate the cationbackbone interaction.

It is reasonable to suggest that similar cation $-\pi$ interactions may be operative in the concentrated phase of PFPI samples in the absence of NaPSS, which should lead to a similar ordering of the average PL lifetime across the cation series. We evaluated this for a few select salt concentrations in the high

salt concentration limit (Table S2). We find that for most samples, lifetimes in the presence of KBr and CsBr are longer than those with LiBr. However, this is not universally true as the 5.0 M LiBr sample shows the longest PL lifetime. Interestingly, this sample distinguishes itself based on the visual appearance of the concentrated phase, which looks more liquid. This is also borne out in the corresponding microscopy image (Figure S1D). Thus, although there are similarities in PL lifetime trends between the concentrated phases of PFPI alone and in the complex with NaPSS, there are some compelling differences. A deeper investigation into CPE behavior in the absence of an oppositely charged polyelectrolyte and at large [LiBr] will be the subject of future work.

In addition to polarizability, differences in hydration radius also need to be considered as a possible factor in TRPL differences of the PFPI/NaPSS complex in the presence of LiBr relative to both KBr and CsBr. The hydration radius could play a direct role in the ability of a cation to enter, swell, and disrupt complexation. It is possible that the small radius of Li⁺ ion could allow it to infiltrate the complex to a comparable extent as K⁺ and Cs⁺ but without a comparable disruption in the CPE π – π interactions. However, the hydration radius is in fact the largest for Li⁺ at ~3.8 Å and comparable for K⁺ and Cs⁺ at ~3.3 Å. This idea is consistent with K⁺ and Cs⁺, leading to similar results, particularly when compared to Li⁺. Thus, differences in hydrated ion radii are unlikely to be the main reason for our TRPL trends, further bolstering the primary role of the cation– π interaction in these observations.

Putting it all together, we attribute the increase in PL lifetime for KBr and CsBr relative to LiBr as resulting from a partial break-up of H-like exciton states associated with interchromophore interactions. This is due to the increase in relative proximity of K^+ and Cs^+ to the CPE backbone and increased cation— π interactions. The combination of rheological and TRPL results leads us to propose that the larger size of hydrated Li⁺ ions may also partially hinder infiltration of the polyelectrolyte complex leading to a significantly smaller disruption of π -stacking interactions, in contrast to the K^+ and Cs^+ ions.

These specific ion interactions and variations of solvation energy between ion types play a major role in the ordering of ions in the well-known Hoffmeister series involving protein solubility, leading to "salting-in" and "salting-out" phenomena. However, it is well established that different macroions lead to different ion orderings along the Hoffmeister series. Because of this and the additional complexity that a CPE presents, our focus in this work was instead on a limited series of simple cations, deliberately avoiding more complex molecular ions. In the future, it will be of fundamental interest to expand the scope of the phase behavior and photophysical investigation across the entirety of an effective Hoffmeister ion series.

An aqueous, coacervate-like CPE-based concentrated phase has intriguing light-harvesting implications. We hypothesized that the delocalized π -electrons of a CPE backbone could in principle recruit other nonpolar π -conjugated organic semiconductors into the concentrated phase. Such molecules would otherwise have a vanishing propensity to infiltrate the polyelectrolyte-rich aqueous phase unless the molecules were polar or ionically charged. As a proof of principle, we used a quintessential fullerene derivative, PC[70]BM, to test our hypothesis. This fullerene derivative is part of a family of the most well-studied photoinduced electron acceptors. This molecule has been used to efficiently convert excitons on

conjugated polymers to spatially separated electron/hole pairs in thin-film organic solar cells. 44-47 PC[70]BM is highly soluble in organic solvents, such as chloroform or chlorobenzene, used to cast solar cell thin films; it has near-zero solubility in water. If PFPI can in fact recruit PC[70]BM to be in the vicinity of the CPE backbone, we expect that PL from PFPI excitons will become partially quenched primarily *via* photoinduced electron transfer to PC[70]BM. This should give rise to a decrease in the average PL lifetime of PFPI.

The effects of exposing the PFPI/NaPSS concentrated phase to PC[70]BM were analyzed by calculating the PL quenching ratio, Q, for each sample, defined by

$$Q = 1 - \int_0^\infty I_{\mathbf{q}}(t) dt / \int_0^\infty I_{\mathbf{n}\mathbf{q}}(t) dt$$
 (7)

where $I_{\rm q}(t)$ is the deconvolved PFPI PL decay after exposure to organic PC[70]BM solutions and $I_{\rm nq}(t)$ is the corresponding decay of the control (non-quenched) sample not exposed to PC[70]BM solution. Figure S9A shows a bar graph of Q for the different conditions that we explored. A plot of the decays, fits, and deconvolution parameters are reported in Figure S8 and Table S3. We observe a notable color change of the concentrated phase to a light opaque brown. Compared to corresponding controls, the CPE PL is quenched in all samples exposed to PC[70]BM (Figure S8A,B).

When compared to the unheated 3.5 M KBr control, the most significant quenching was found to occur for the CHCl₃ sample with a $Q \sim 39\%$. Though a more thorough investigation is warranted, this result is interesting for two reasons. First, it appears that the organic solvent used to dissolve PC[70]BM had a measurable influence on the probability of PC[70]BM transfer into the coacervate. Second, given that the fullerene derivative does not contain functional groups expected to promote aqueous solubility, the maximal quenching that we observe is quite substantial. A judicious choice of functionalization pattern of the photoinduced electron acceptor will very likely lead to a significant further increase in quenching. Thus, we believe that the fullereneinfiltrated CPE-based coacervate can be manipulated to produce photoinduced electron/hole pairs at the CPE/ fullerene interface with impressive rates. A cartoon of the fullerene-infiltrated system is shown in Figure S9B. Future work will systematically investigate the fullerene/CPE interaction in detail, including the role of the non-conjugated polyelectrolyte component.

5. CONCLUSIONS

We have shown that CPEs can undergo aqueous associative phase separation into a diluted and concentrated phase, which shows evidence of complex coacervation. However, we have also shown that the phase behavior is more complex than pure liquid/liquid phase separation and likely corresponds to formation of a colloidal gel. We found that the photophysical properties of the concentrated phase depended on the nature of the excess salt ions, allowing us to manipulate the radiative relaxation and exciton diffusion dynamics. Using time-resolved PL anisotropy measurements, we showed that the concentrated phase is spatially heterogeneous with depolarization times that depend on the ion type. Our work raises interesting questions about the possibility of using the nature of the ion to tune the coupling between phase behavior and photophysical properties of complex fluids. It is particularly intriguing to ask whether the presence of molecular ions can both lead to the

formation of pure liquid—liquid phase separation and tune the optical properties of the fluid.

The ability to form a coacervate-like CPE state also has interesting implications for light-harvesting applications. Specifically, we showed that a model nonpolar, fullerene-based electron acceptor can be infiltrated into the concentrated phase, leading to PL quenching likely by photoinduced electron transfer. Our work suggests that liquid electron donor/acceptor bulk heterojunctions may be formed in aqueous solution, which may serve as photochemical reaction media or sensing platforms for high ionic-strength environments.

ASSOCIATED CONTENT

Supporting Information

The Supporting Information is available free of charge at https://pubs.acs.org/doi/10.1021/acs.chemmater.0c02424.

PL microscopy, UV-vis spectra, ICP-OES results, rheology, time-resolved PL for both complexes and phase-separated solutions containing only the CPE, and time-resolved PL anisotropy measurements taken at different sample settling times (PDF)

AUTHOR INFORMATION

Corresponding Author

Alexander L. Ayzner — Department of Chemistry and Biochemistry, University of California Santa Cruz, Santa Cruz, California 95064, United States; oorcid.org/0000-0002-6549-4721; Email: aayzner@ucsc.edu

Authors

Anna R. Johnston – Department of Chemistry and Biochemistry, University of California Santa Cruz, Santa Cruz, California 95064, United States

Sarah L. Perry — Department of Chemical Engineering, University of Massachusetts Amherst, Amherst, Massachusetts 01003, United States; orcid.org/0000-0003-2301-6710

Complete contact information is available at: https://pubs.acs.org/10.1021/acs.chemmater.0c02424

Notes

The authors declare no competing financial interest.

ACKNOWLEDGMENTS

This material is based upon work supported by the National Science Foundation under grant no. 1848069 and the ACS Petroleum Research Fund New Directions (grant no. 60244-ND7). This material is also based upon work supported by the National Science Foundation Graduate Research Fellowship under grant no. DGE-1842400. Part of this work was performed at the Stanford Nano Shared Facilities (SNSF), supported by the National Science Foundation under award ECCS-1542152. We would also like to thank Dr. Carmen Segura and Dr. Brian Dreyer for their helpful discussions regarding this work.

REFERENCES

- (1) Dubin, P.; Stewart, R. J. Complex Coacervation. Soft Matter 2018, 14, 329-330.
- (2) Fu, J.; Schlenoff, J. B. Driving Forces for Oppositely Charged Polyion Association in Aqueous Solutions: Enthalpic, Entropic, but Not Electrostatic. *J. Am. Chem. Soc.* **2016**, *138*, 980–990.

- (3) Fu, J.; Fares, H. M.; Schlenoff, J. B. Ion-Pairing Strength in Polyelectrolyte Complexes. *Macromolecules* **2017**, *50*, 1066–1074.
- (4) Schlenoff, J. B. Non-Equilibrium Phenomena and Kinetic Pathways in Self-Assembled Polyelectrolyte Complexes. *J. Chem. Phys.* **2018**, *149*, 163314.
- (5) Tirrell, M. Polyelectrolyte Complexes: Fluid or Solid? *ACS Cent. Sci.* **2018**, *4*, 532–533.
- (6) Marciel, A. B.; Srivastava, S. S.; Tirrell, M. V. Structure and Rheology of Polyelectrolyte Complex Coacervates[†]. *Soft Matter* **2018**, *14*, 2454.
- (7) Sing, C. E.; Perry, S. L. Recent Progress in the Science of Complex Coacervation. *Soft Matter* **2020**, *16*, 2885–2914.
- (8) Keating, C. D. Aqueous Phase Separation as a Possible Route to Compartmentalization of Biological Molecules. *Acc. Chem. Res.* **2012**, 45, 2114.
- (9) Alberti, S.; Gladfelter, A.; Mittag, T. Considerations and Challenges in Studying Liquid-Liquid Phase Separation and Biomolecular Condensates. *Cell* **2019**, *176*, 419–434.
- (10) Martin, N. Dynamic Synthetic Cells Based on Liquid-Liquid Phase Separation. *ChemBioChem* **2019**, *20*, 2553–2568.
- (11) Black, K. A.; Priftis, D.; Perry, S. L.; Yip, J.; Byun, W. Y.; Tirrell, M. Protein Encapsulation via Polypeptide Complex Coacervation. *ACS Macro Lett.* **2014**, *3*, 1088–1091.
- (12) Rumyantsev, A. M.; Zhulina, E. B.; Borisov, O. V.; Petersburg, S. Complex Coacervate of Weakly Charged Polyelectrolytes: Diagram of States. *Macromolecules* **2018**, *51*, 3788–3801.
- (13) Messaoud, G. B.; Promeneur, L.; Brennich, M.; Roelants, S. L. K. W.; Le Griel, P.; Baccile, N. Complex Coacervation of Natural Sophorolipid Bolaamphiphile Micelles with Cationic Polyelectrolytes †. *Green Chem.* **2018**, *20*, 3371–3385.
- (14) Krogstad, D. V.; Lynd, N. A.; Choi, S.-H.; Spruell, J. M.; Hawker, C. J.; Kramer, E. J.; Tirrell, M. V. Effects of Polymer and Salt Concentration on the Structure and Properties of Triblock Copolymer Coacervate Hydrogels. *Macromolecules* **2013**, *46*, 1512–1518.
- (15) Danielsen, S. P. O.; Nguyen, T.-Q.; Fredrickson, G. H.; Segalman, R. A. Complexation of a Conjugated Polyelectrolyte and Impact on Optoelectronic Properties. *ACS Macro Lett.* **2019**, *8*, 88–
- (16) Nakashima, K. K.; Vibhute, M. A.; Spruijt, E. Biomolecular Chemistry in Liquid Phase Separated Compartments. *Front. Mol. Biosci.* **2019**, *6*, 21.
- (17) Aumiller, W. M.; Pir Cakmak, F.; Davis, B. W.; Keating, C. D. RNA-Based Coacervates as a Model for Membraneless Organelles: Formation, Properties, and Interfacial Liposome Assembly. *Langmuir* **2016**, 32, 10042–10053.
- (18) Hollingsworth, W. R.; Magnanelli, T. J.; Segura, C.; Young, J. D.; Bragg, A. E.; Ayzner, A. L. Polyion Charge Ratio Determines Transition between Bright and Dark Excitons in Donor/Acceptor-Conjugated Polyelectrolyte Complexes. J. Phys. Chem. C 2018, 122, 22280–22293.
- (19) Ludescher, R. D.; Peting, L.; Hudson, S.; Hudson, B. Time-Resolved Fluorescence Anisotropy for Systems with Lifetime and Dynamic Heterogeneity. *Biophys. Chem.* **1987**, 28, 59–75.
- (20) Addison, C. C. Inorganic Chemistry of the Main-Group Elements. R. Soc. Chem. 1977, 4, 13–17.
- (21) Sternheimer, R. M. Electronic Polarizabilities of Ions from the Hartree-Fock Wave Functions. *Phys. Rev.* **1954**, *96*, 951–968.
- (22) Spruijt, E.; Westphal, A. H.; Borst, J. W.; Cohen Stuart, M. A.; Van Der Gucht, J. Binodal Compositions of Polyelectrolyte Complexes. *Macromolecules* **2010**, *43*, 6476–6484.
- (23) Li, L.; Srivastava, S.; Andreev, M.; Marciel, A. B.; De Pablo, J. J.; Tirrell, M. V. Phase Behavior and Salt Partitioning in Polyelectrolyte Complex Coacervates. *Macromolecules* **2018**, *51*, 2988–2995.
- (24) Liu, Y.; Momani, B.; Winter, H. H.; Perry, S. L. Rheological Characterization of Liquid-to-Solid Transitions in Bulk Polyelectrolyte Complexes†. *Soft Matter* **2017**, *13*, 7332.
- (25) Spruijt, E.; Sprakel, J.; Lemmers, M.; Cohen Stuart, M. A.; Van Der Gucht, J. Relaxation Dynamics at Different Time Scales in

Electrostatic Complexes: Time-Salt Superposition. *Phys. Rev. Lett.* **2010**, *105*, 208301.

- (26) Liu, Y.; Winter, H. H.; Perry, S. L. Linear Viscoelasticity of Complex Coacervates. *Adv. Colloid Interface Sci.* **2017**, 239, 46–60.
- (27) Wang, Q.; Schlenoff, J. B. The Polyelectrolyte Complex/Coacervate Continuum. *Macromolecules* **2014**, 47, 3108–3116.
- (28) Spruijt, E.; Stuart, M. A. C.; Van Der Gucht, J. Linear Viscoelasticity of Polyelectrolyte Complex Coacervates. *Macromolecules* **2013**, *46*, 1663–1641.
- (29) Manas, E. S.; Spano, F. C. Absorption and Spontaneous Emission in Aggregates of Conjugated Polymers. *J. Chem. Phys.* **1998**, *109*, 8087–8101.
- (30) Spano, F. C. Modeling Disorder in Polymer Aggregates: The Optical Spectroscopy of Regioregular Poly(3-Hexylthiophene) Thin Films. *J. Chem. Phys.* **2005**, *122*, 234701.
- (31) Lakowicz, J. R. Principles of Fluorescence Spectroscopy, 3rd ed.; Springer Science + Business Media, LLC, 2006.
- (32) Smith, T. A.; Ghiggino, K. P. A Review of the Analysis of Complex Time-Resolved Fluorescence Anisotropy Data. *Methods Appl. Fluoresc.* **2015**, *3*, 022001.
- (33) Fayer, M. D.; Levinger, N. E. Analysis of Water in Confined Geometries and at Interfaces. *Annu. Rev. Anal. Chem.* **2010**, *3*, 89–107.
- (34) Ma, J. C.; Dougherty, D. A. The Cation- π Interaction. *Chem. Rev.* **1997**, 97, 1303–1324.
- (35) Mahadevi, A. S.; Sastry, G. N. Cation $-\pi$ Interaction: Its Role and Relevance in Chemistry, Biology, and Material Science. *Chem. Rev.* **2012**, *113*, 2100–2138.
- (36) Schyman, P.; Jorgensen, W. L. Exploring Adsorption of Water and Ions on Carbon Surfaces Using a Polarizable Force Field. *J. Phys. Chem. Lett.* **2013**, *4*, 468–474.
- (37) Kumpf, R.; Dougherty, D. A Mechanism for Ion Selectivity in Potassium Channels: Computational Studies of Cation- π . *Science* **1993**, 261, 1708–1710.
- (38) Salomon, M. The Thermodynamics of Ion Solvation in Water and Propylene Carbonate. J. Phys. Chem. 1970, 74, 2519–2524.
- (39) Cabarcos, O. M.; Weinheimer, C. J.; Lisy, J. M. Competitive Solvation of by Benzene and Water: Cation- π Interactions and π -Hydrogen Bonds. *J. Chem. Phys.* **1998**, *108*, 5151.
- (40) Barford, W.; Tozer, O. R. Theory of Exciton Transfer and Diffusion in Conjugated Polymers. J. Chem. Phys. 2014, 141, 164103.
- (41) Barford, W.; Marcus, M. Theory of Optical Transitions in Conjugated Polymers. I. Ideal Systems. *J. Chem. Phys.* **2014**, *141*, 164101.
- (42) Marcus, M.; Tozer, O. R.; Barford, W. Theory of Optical Transitions in Conjugated Polymers. II. Real Systems. *J. Chem. Phys.* **2014**, *141*, 164102.
- (43) Tozer, O. R.; Barford, W. Intrachain Exciton Dynamics in Conjugated Polymer Chains in Solution. *J. Chem. Phys.* **2015**, *143*, 084102.
- (44) Liu, T.; Troisi, A. What Makes Fullerene Acceptors Special as Electron Acceptors in Organic Solar Cells and How to Replace Them. *Adv. Mater.* **2013**, *25*, 1038–1041.
- (45) Loi, M. A.; Toffanin, S.; Muccini, M.; Forster, M.; Scherf, U.; Scharber, M. Charge Transfer Excitons in Bulk Heterojunctions of a Polyfluorene Copolymer and a Fullerene Derivative. *Adv. Funct. Mater.* **2007**, *17*, 2111–2116.
- (46) Kim, D. H.; Ayzner, A. L.; Appleton, A. L.; Schmidt, K.; Mei, J.; Toney, M. F.; Bao, Z. Comparison of the Photovoltaic Characteristics and Nanostructure of Fullerenes Blended with Conjugated Polymers with Siloxane-Terminated and Branched Aliphatic Side Chains. *Chem. Mater.* **2013**, 25, 431–440.
- (47) Wei, G.; Wang, S.; Sun, K.; Thompson, M. E.; Forrest, S. R. Solvent-Annealed Crystalline Squaraine: PC70BM (1:6) Solar Cells. *Adv. Energy Mater.* **2011**, *1*, 184–187.
- (48) Marcus, Y. Ionic Radii in Aqueous Solutions. *Chem. Rev.* **1988**, 88, 1475–1498.
- (49) Puertas, A. M. Dynamical Heterogeneities Close to a Collodial Gel. J. Chem. Phys. 2004, 121, 2813.

- (50) Nightingale, E. R., Jr. Phenominological Theory of Ion Solvation. J. Phys. Chem. 1959, 63, 1381–1387.
- (51) Israelachvili, J. N. *Intermolecular and Surface Forces*, 3rd ed.; Elsevier Science and Technology, 2011; pp 71–88.
- (52) Pham, T. A.; Mortuza, S. M. G.; Wood, B. C.; Lau, E. Y.; Ogitsu, T.; Buchsbaum, S. F.; Siwy, Z. S.; Fornasiero, F.; Schwegler, E. Salt Solutions in Carbon Nanotubes: The Role of Cation- π Interactions. *J. Phys. Chem. C* **2016**, 120, 7332–7338.
- (53) Williams, C. D.; Dix, J.; Troisi, A.; Carbone, P. Effective Polarization in Pairwise Potentials at the Graphene-Electrolyte Interface. *J. Phys. Chem. Lett.* **2017**, *8*, 703–708.